



A phase-resolved, depth-averaged non-hydrostatic numerical model for cross-shore wave propagation

Xinhua Lu^{a,*}, Xiaofeng Zhang^a, Bing Mao^b, Bingjiang Dong^c

^a State Key Laboratory of Water Resources and Hydropower Engineering Science, Wuhan University, Wuhan 430072, China

^b Yangtze River Scientific Research Institute, Wuhan 430015, China

^c Hydrology Bureau, Yangtze River Water Resource Commission, Wuhan 430010, China

ARTICLE INFO

Article history:

Received 26 June 2015

Accepted 14 September 2015

Available online 11 November 2015

Keywords:

Non-hydrostatic

Dispersivity

Wave breaking

Well-balanced

Shock-capturing

HLL

ABSTRACT

In this study, a phase-resolved and depth-averaged non-hydrostatic numerical model (SNH model) is developed. The non-incremental pressure-correction method is employed to solve the equation system in two successive steps. Firstly, an approximate Riemann solver in the framework of finite volume methods is employed to solve the hydrostatic shallow-water equations (SWE) on a collocated grid to obtain provisional solutions. Then, the intermediate solutions is updated by considering the non-hydrostatic pressure effect; a semi-staggered grid is used in this step to avoid predicting checkboard pressure field. A series of benchmark tests are used to validate the numerical model, showing that the developed model is well-balanced and describes the wetting and drying processes accurately. By employing a shock-capturing numerical scheme, the wave-breaking phenomenon is reasonably simulated without using any ad-hoc techniques. Compared with the SWE model, the wave shape can be well-preserved and the numerical predictions are much improved by using the SNH model.

© 2015 Académie des sciences. Published by Elsevier Masson SAS. All rights reserved.

1. Introduction

The surf-zone and inner-shelf regions are of paramount importance for human beings. Accurate prediction of the flow motions in these regions is vital for designing and protecting engineering projects and is the basis for building early tsunami warning systems [1,2]. Besides, the prediction of flow features in these regions is important for studying coastal sediment transport and the associated beach profile changes [3–5].

For modeling the cross-shore hydrodynamics, phase-resolved and depth-averaged models are widely adopted. These models include the ones solving the nonlinear shallow-water equations (SWE), the Boussinesq-type equations (BTE) and the depth-averaged non-hydrostatic shallow-water equations (SNH). Of all the three types of models, the recently proposed SNH model framework [6] seems to be very promising. Firstly, compared with the SWE, which does not account for the wave dispersion effect, the SNH can represent weak wave dispersivity and thus is suitable for modeling long wave as well as short wave motions. Secondly, to simulate the wave-breaking phenomenon, which is commonly seen in the nearshore area, the BTE model generally requires an ad-hoc technique to numerically dissipate the wave energy during the wave-breaking process; in this regard, an artificial viscosity term [7,8] or a surface roller model [9,10], or a local switch from resolving the BTE to SWE in the vicinity of the breaking wave fronts [11–13], is widely used. Compared with a BTE model, the SNH

* Corresponding author.

E-mail address: xhluhh@whu.edu.cn (X. Lu).

model has the potential to handle the wave-breaking process well when a shock-capturing numerical scheme is employed. Besides, the BTE contains high-order spatial derivatives that are difficult for numerical implementations, while for the SNH, the order of derivatives is generally one (when the diffusion terms are omitted) and thus easier for numerical realizations.

To date, very few SNH models have been developed and, among them, most are developed using the finite-difference method [6,14] or the finite-element method [15,16]. In viewing that the finite-volume Godunov-type schemes devised based on the hyperbolic conservation laws generally intrinsically have the shock-capturing property, in this study, we aim to develop a SNH model based on the finite-volume Godunov-type scheme to adapt to wave-breaking simulations without using any ad-hoc techniques. Also, the well-balanced property (e.g., the C-property) for the existing SNH models is generally not verified and in this work the developed SNH model will achieve this property. Note that it is important for a numerical scheme to satisfy the well-balanced requirement to accurately predict the wave phase speeds and the flow motions involving wetting and drying processes [17,18].

The rest of the paper is organized as follows. Section 2 presents the governing equations and the numerical algorithm for the SNH model. The specially designed grid layout and the essentials for the numerical discretizations are demonstrated. In Section 3, numerical tests are used to verify the various properties of the numerical model. Finally, conclusions and discussions are given in Section 4.

2. Numerical model

2.1. Governing equations

By depth-integrating the vertical 2D Reynolds-averaged Navier–Stokes equations and using the following kinematic boundary conditions at the free surface and water bottom

$$w_s = \frac{\partial z}{\partial t} + u_s \frac{\partial z}{\partial x} \quad (1)$$

$$w_b = u_b \frac{\partial z_b}{\partial x} \quad (2)$$

the governing equations for the 1D SNH model can be derived as follows [6]

$$\frac{\partial z}{\partial t} + \frac{\partial q_x}{\partial x} = 0 \quad (3)$$

$$\frac{\partial q_x}{\partial t} + \frac{\partial}{\partial x} \left(\bar{u}q_x + \frac{1}{2}gh^2 \right) = -gh \frac{\partial z_b}{\partial x} - \frac{gn^2 q_x |q_x|}{h^{7/3}} - \frac{h}{2\rho} \frac{\partial \Gamma_b}{\partial x} - \frac{\Gamma_b}{2\rho} \frac{\partial (z + z_b)}{\partial x} \quad (4)$$

$$\frac{\partial \bar{w}}{\partial t} = \frac{\Gamma_b}{\rho h} \quad (5)$$

Here, t denotes time; x denotes the horizontal coordinate in the cross-shore direction; z and z_b respectively denote the water surface and bed elevations above a horizontal reference level; u and w are the velocity components in the horizontal and vertical directions; the subscripts 's' and 'b' denote the values at the free surface and water bottom, respectively; $h = z - z_b$ denotes the water depth; $q_x = \bar{u} \cdot h$ is the discharge per unit width with $\bar{(\cdot)}$ denoting the depth-averaging operator; Γ_b denotes the non-hydrostatic pressure at the water bottom; $\rho = 1000 \text{ kg/m}^3$ is the density of water; g is the acceleration due to gravity; n is the Manning's roughness coefficient. To be remarked that in the derivations, the non-hydrostatic pressure and the vertical velocity are assumed to vary linearly with water depth [6]; the shear stress at the water bottom (i.e., the bed friction force) is closed by the second term on the right-hand side of Eq. (4). For brevity, the overbar of variables in Eqs. (4) and (5) will be dropped hereafter.

2.2. Numerical algorithm

The non-incremental pressure-correction method is employed for solving the governing equations, which divides the solution into two successive steps, namely, the hydrostatic and non-hydrostatic steps.

2.2.1. Hydrostatic step

In the hydrostatic step, the classic SWE is solved, which in a conservative vector form can be written as

$$\frac{\partial \mathbf{U}}{\partial t} + \frac{\partial \mathbf{F}}{\partial x} = \mathbf{S} \quad (6)$$

where the vectors are defined by

$$\mathbf{U} = \begin{bmatrix} z \\ q_x \end{bmatrix}, \quad \mathbf{F} = \begin{bmatrix} q_x \\ uq_x + \frac{1}{2}gh^2 \end{bmatrix}, \quad \mathbf{S} = \mathbf{S}_0 + \mathbf{S}_f = \begin{bmatrix} 0 \\ -gh \frac{\partial z_b}{\partial x} \end{bmatrix} + \begin{bmatrix} 0 \\ -\frac{gn^2 q_x |q_x|}{h^{7/3}} \end{bmatrix} \quad (7)$$

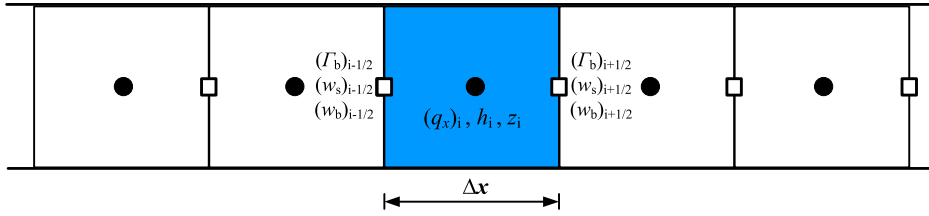


Fig. 1. Sketch of the semi-staggered grid layout.

For the numerical discretization of Eq. (6), a collocated grid is used so that the water surface elevation and the horizontal velocity are defined at the same locations as shown in Fig. 1. Based on the collocated grid, an explicit second-order Runge–Kutta scheme [19] is used for the discretization of Eq. (6) as

$$U_i^{(1)} = U_i^n - \frac{\Delta t}{\Delta x} (F_{i+1/2}^n - F_{i-1/2}^n) + \Delta t (S_0)_i^n \tag{8}$$

$$U_i^{(2)} = \frac{1}{2} U_i^n + \frac{1}{2} U_i^{(1)} - \frac{1}{2} \frac{\Delta t}{\Delta x} (F_{i+1/2}^{(1)} - F_{i-1/2}^{(1)}) + \frac{1}{2} \Delta t (S_0)_i^{(1)} \tag{9}$$

$$U_i^m = U_i^{(2)} + \Delta t S_f(U_i^n, U_i^m) \tag{10}$$

Here, the subscript ‘i’ denotes the cell index; the superscript ‘n’ denotes the value at the last time step, and ‘(1)’, ‘(2)’ and ‘m’ denote the intermediate values. The point implicit method [20] is employed for discretizing the friction source terms in Eq. (10).

The numerical fluxes in Eqs. (8) and (9) are computed by using the HLL approximate Riemann solver [21]. For the 1D problem, the HLL scheme is equivalent to the HLLC scheme [22] and reads

$$F_{i-1/2} = \begin{cases} F_{i-1/2}^L & 0 \leq \xi_{i-1/2}^L \\ \frac{\xi^R F^L - \xi^L F^R + \xi^L \xi^R (U^R - U^L)}{\xi^R - \xi^L} \Big|_{i-1/2} & \xi_{i-1/2}^L \leq 0 \leq \xi_{i-1/2}^R \\ F_{i-1/2}^R & \xi_{i-1/2}^R \leq 0 \end{cases} \tag{11}$$

where $F^L = F(U^L)$ and $F^R = F(U^R)$; ξ denotes wave speeds. The superscripts ‘L’ and ‘R’ mean that the variables are related to the Riemann states at the left and right sides of the cell interface. In this work, the Riemann states at the cell interface are reconstructed by using the hydrostatic-reconstruction approach proposed by Audusse et al. [23]; to achieve the second-order accuracy in space, the MUSCL piecewise linear reconstruction method [24] with the minmod slope limiter [25] is employed.

The source term $-gh \frac{\partial z_b}{\partial x}$ in Eq. (7) is discretized as

$$-gh \frac{\partial z_b}{\partial x} \Big|_i = -g \frac{h_{i-1/2}^R + h_{i+1/2}^L}{2} \frac{(z_b)_{i+1/2} - (z_b)_{i-1/2}}{\Delta x} \tag{12}$$

where $(z_b)_{i-1/2} = \max(z_{i-1/2}^L - h_{i-1/2}^L, z_{i-1/2}^R - h_{i-1/2}^R)$. Following the same procedures as done by Audusse et al. [23], one can easily prove that when the HLL solver is used for flux evaluations, the hydrostatic-reconstruction approach along with the source term discretized by Eq. (12) leads to a well-balanced numerical scheme for solving the SWE (Eq. (6)) under quiescent flow conditions.

The wave speeds in Eq. (11) are evaluated as [26]

$$\xi^L = \begin{cases} u^R - 2\sqrt{gh^R}, & \text{if } h^L = 0 \\ \min(u^L - \sqrt{gh^L}, u^* - \sqrt{gh^*}), & \text{if } h^L > 0 \end{cases} \tag{13a}$$

$$\xi^R = \begin{cases} u^L + 2\sqrt{gh^L}, & \text{if } h^R = 0 \\ \max(u^R + \sqrt{gh^R}, u^* + \sqrt{gh^*}), & \text{if } h^R > 0 \end{cases} \tag{13b}$$

Here, u^* and h^* are calculated respectively by

$$u^* = \frac{1}{2} (u^L + u^R) + \sqrt{gh^L} - \sqrt{gh^R} \tag{14}$$

$$h^* = \frac{1}{g} \left[\frac{1}{2} (\sqrt{gh^L} + \sqrt{gh^R}) + \frac{1}{4} (u^L - u^R) \right]^2 \tag{15}$$

2.2.2. Non-hydrostatic step

In this step, the provisional solutions obtained from the first step are updated by solving the following semi-discretized equations

$$\frac{z_i^{n+1} - z_i^m}{\Delta t} + \frac{\partial \Delta q_x}{\partial x} \Big|_i = 0 \tag{16}$$

$$\frac{(q_x)_i^{n+1} - (q_x)_i^m}{\Delta t} = - \frac{h_i^m}{2\rho} \frac{\partial \Gamma_b^{n+1}}{\partial x} \Big|_i - \frac{(\Gamma_b)_i^{n+1}}{2\rho} \frac{\partial (z_i^m + (z_b)_i)}{\partial x} \tag{17}$$

$$\frac{w_{i-1/2}^{n+1} - w_{i-1/2}^n}{\Delta t} = \frac{(\Gamma_b)_{i-1/2}^{n+1}}{\rho h_{i-1/2}^m} \tag{18}$$

Here, $\Delta q_x = q_x^{n+1} - q_x^m$.

To couple the velocity (discharge per unit width) and the non-hydrostatic pressure in Eq. (17) to avoid predicting checker-board pressure field [27], a semi-staggered grid is used. As demonstrated in Fig. 1, the non-hydrostatic pressure and the vertical velocities are defined at the cell interfaces. Based on the semi-staggered grid, the spatial gradient $\frac{\partial \Gamma_b}{\partial x}$ in Eq. (17) is discretized with a second-order central difference scheme, and Eq. (17) then becomes

$$\begin{aligned} \frac{(q_x)_i^{n+1} - (q_x)_i^m}{\Delta t} = & - \frac{h_i^m}{2\rho} \frac{(\Gamma_b)_{i+1/2}^{n+1} - (\Gamma_b)_{i-1/2}^{n+1}}{\Delta x} \\ & - \frac{0.5[(\Gamma_b)_{i+1/2}^{n+1} + (\Gamma_b)_{i-1/2}^{n+1}]}{2\rho} \frac{\partial (z_i^m + (z_b)_i)}{\partial x} \end{aligned} \tag{19}$$

With the linear assumption for w in the vertical direction, Eq. (18) can be discretized as

$$\frac{(w_s)_{i-1/2}^{n+1} + (w_b)_{i-1/2}^{n+1} - (w_s)_{i-1/2}^n - (w_b)_{i-1/2}^n}{2\Delta t} = \frac{(\Gamma_b)_{i-1/2}^{n+1}}{\rho h_{i-1/2}^m} \tag{20}$$

Note that the interface value $h_{i-1/2}^m$ in Eq. (20) and the partial derivative term $\frac{\partial (z_i^m + (z_b)_i)}{\partial x}$ in Eq. (19) are evaluated by an upwind scheme to ensure stability. For instance, the $h_{i-1/2}^m$ is calculated as

$$h_{i-1/2}^m = \frac{1 + \text{sgn}(u_f)}{2} h_{i-1}^m + \frac{1 - \text{sgn}(u_f)}{2} h_i^m \tag{21}$$

where $u_f = 0.5(u_{i-1}^m + u_i^m)$.

Eqs. (19) and (20) contain two equations but with four independent variables, namely, q_x^{n+1} , Γ_b^{n+1} , w_s^{n+1} and w_b^{n+1} . To close the solution, the following two steps are taken. Firstly, following Walters [15], and Wei and Jia [16], the vertical velocity at the water bottom is estimated from Eq. (2), which in a discretized form is

$$(w_b)_i^{n+1} \approx u_{i-1/2}^m \frac{(z_b)_i - (z_b)_{i-1}}{\Delta x} \tag{22}$$

where the interface value $u_{i-1/2}^m$ is determined according to Eq. (21). Note that the boundary layer is not resolved by the current depth-averaged model, and thus Eq. (22) can be viewed as an estimation of the vertical velocity immediately outside the boundary layer [28]. Secondly, the velocity field is enforced to satisfy the divergence-free condition, which in a discretized form gives:

$$\frac{u_i^{n+1} - u_{i-1}^{n+1}}{\Delta x} + \frac{(w_s)_{i-1/2}^{n+1} - (w_b)_{i-1/2}^{n+1}}{h_{i-1/2}^m} = 0 \tag{23}$$

By assuming $(q_x)_i^{n+1} \approx u_i^{n+1} h_i^m$ and with some mathematical manipulations, the following tridiagonal system for Γ_b^{n+1} can be derived from Eqs. (19), (20) and (23):

$$A_{i-1/2} (\Gamma_b)_{i-3/2}^{n+1} + B_{i-1/2} (\Gamma_b)_{i-1/2}^{n+1} + C_{i-1/2} (\Gamma_b)_{i+1/2}^{n+1} = S_{i-1/2} \tag{24}$$

The detailed derivation for Eq. (24) and the coefficients $A_{i-1/2}$, $B_{i-1/2}$, $C_{i-1/2}$ and $S_{i-1/2}$ are given in Appendix A. For solving Eq. (24), when Dirichlet boundary conditions are prescribed at both ends of the simulation domain, the tridiagonal matrix algorithm (TDMA) is used; otherwise, a preconditioned biconjugate gradient stabilized (Bi-CGSTAB) method [29] is invoked. Once Γ_b^{n+1} is solved, q_x^{n+1} and w_s^{n+1} are computed from Eqs. (19) and (20), respectively. Then, the water level z^{n+1} is updated through Eq. (16), which in a discretized form can be written as

$$\frac{z_i^{n+1} - z_i^m}{\Delta t} + \frac{\Delta q_x|_{i+1} - \Delta q_x|_{i-1}}{2\Delta x} = 0 \tag{25}$$

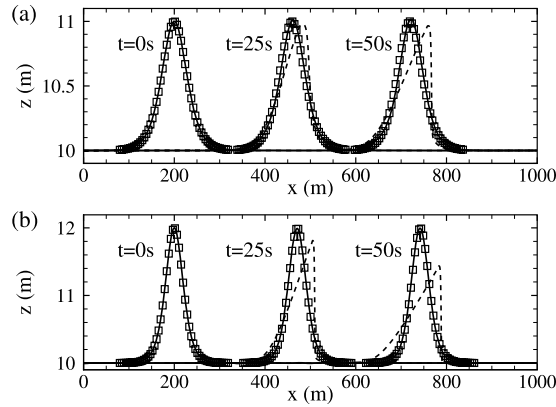


Fig. 2. Computed water surface profiles at different time instances by the SNH model (—) and SWE model (---) for solitary waves propagating over a constant water depth channel with $H/d = 0.1$ (a) and $H/d = 0.2$ (b). The analytic solutions are given in symbols (\square).

2.2.3. Boundary conditions and stability criteria

For treatment of the boundary conditions, ghost cells are created outside the simulation domain. For an open boundary condition, all the variables in the relevant ghost cells are zeroth-order extrapolated from interior cells. For a closed boundary condition, the discharges in the relevant ghost cells are set to equal but opposite to the value in its neighboring interior cells, while the water depth at the ghost cells is set to the value in the adjacent interior cells. At the inlet boundary, $\Gamma_b = 0$ is prescribed; this is reasonable as the flow at the inlet boundary is weak for all the tests considered in this work and thus the non-hydrostatic pressure effect there can be omitted. When the flow cannot reach the outlet boundary during the simulation, we impose $\Gamma_b = 0$ in the relevant ghost cells to accelerate the solution to the pressure elliptic equation by using the TDMA solver (more efficient than the Bi-CGSTAB solver); otherwise, $\frac{\partial \Gamma_b}{\partial x} = 0$ is imposed and the Bi-CGSTAB solver is utilized.

A dynamic time step is used in the simulations according to the CFL condition:

$$\Delta t = C_r \times \min \left(\frac{\Delta x}{|u_i^n| + \sqrt{gh_i^n}} \right) \quad (26)$$

where the coefficient C_r should be specified.

3. Numerical tests

In this section, several benchmark tests are used to verify the performance of the developed numerical model. In all the tests, $g = 9.81 \text{ m/s}^2$ applies.

3.1. Solitary waves propagating over a constant water depth channel

In this test, solitary waves propagating over a constant water depth and 1000-m-long channel are simulated. The considered channel is frictionless and thus the solitary wave should travel with a constant wave phase speed and meanwhile maintain its initial shape. We consider two test cases with different wave-height-to-water-depth ratios, $H/d = 0.1$ and $H/d = 0.2$. Here, H denotes the initial wave height of the solitary wave; d is the still water depth and chosen as 10 m.

Initially, the water surface elevation and velocity components are prescribed according to

$$z(x, t) = d + H \operatorname{sech}^2 \left[\sqrt{\frac{3H}{4d^3}} (x - ct - X_s) \right] \quad (27)$$

$$u(x, t) = \frac{c(z(x, t) - d)}{h(x, t)} \quad (28)$$

$$w_s(x, t) = -z(x, t) \frac{\partial u(x, t)}{\partial x} \quad (29)$$

where $c \approx \sqrt{g(H+d)}$ is the wave phase speed; X_s is the center of the initial solitary wave and is set to 200 m. In the simulations, a uniform mesh with 2000 mesh cells and $C_r = 0.5$ are employed. Open boundary conditions are imposed at both ends of the simulation domain.

Fig. 2 displays the water surface profiles computed by the SWE and SNH models at various time instances for the two test cases. The analytic solutions (described by Eqs. (27)–(29)) are also shown. It is obvious that the wave shape is accurately

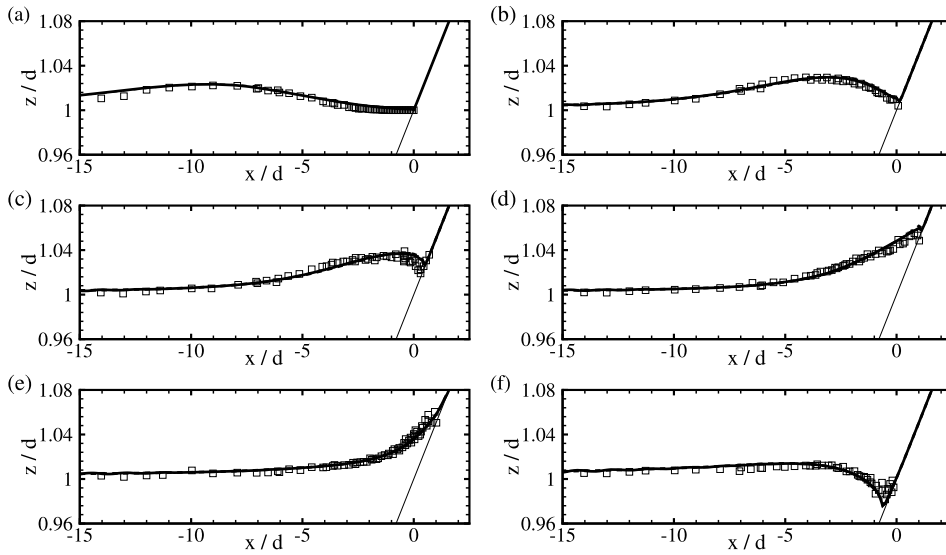


Fig. 3. Computed water surface profiles at $\tilde{t} = 30$ (a), $\tilde{t} = 40$ (b), $\tilde{t} = 45$ (c), $\tilde{t} = 50$ (d), $\tilde{t} = 60$ (e) and $\tilde{t} = 70$ (f). The thick solid (—) and dashed (---) lines represent the solutions by the SNH and SWE models, respectively. The symbols (\square) show the experimental data by Synolakis [30]. The thin solid line represents the bed topography.

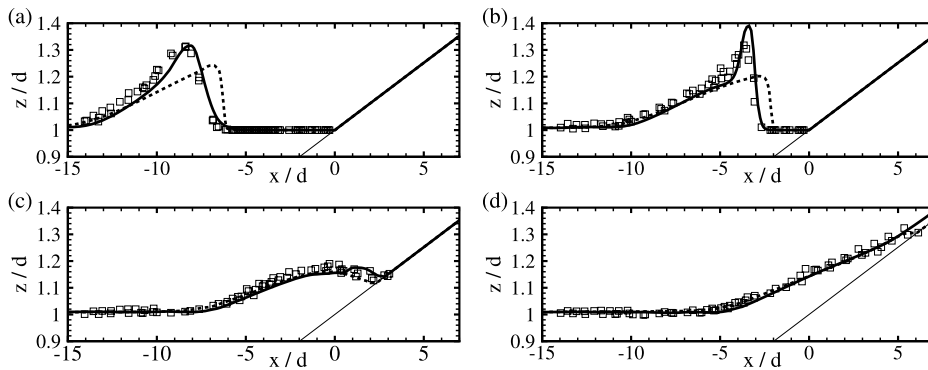


Fig. 4. Computed water surface profiles at $\tilde{t} = 15$ (a), $\tilde{t} = 20$ (b), $\tilde{t} = 25$ (c) and $\tilde{t} = 30$ (d). The thick solid (—) and dashed (---) lines represent the solutions by the SNH and SWE models, respectively. The symbols (\square) show the experimental data by Synolakis [30]. The thin solid line represents the bed topography.

preserved by the SNH model for both test cases. However, the SWE model predicts unsymmetrical wave profiles and the predicted wave amplitudes are smaller than the analytic values (especially for the $H/d = 0.2$ test case).

3.2. Solitary waves running up and down a plane beach

In this test, we consider solitary waves running up and down a sloped beach, which were experimentally investigated by Synolakis [30]. The simulation domain is comprised of two parts: in the region $x/d > -19.85$, there is a plane beach with slope 1 : 19.85 and in the other region, the flume bottom is flat ($z_b = 0$). Here, the origin ($x = 0$) is defined at a location where the horizontal line at an elevation of d intersects the beach surface. Two test cases with $H/d = 0.0185$ and $H/d = 0.28$ are considered. For the highly nonlinear test case ($H/d = 0.28$), the wave broke in the experiment while it was not for the weak nonlinear case ($H/d = 0.0185$). In the simulations, the initial conditions are prescribed according to Eqs. (27)–(29). The solitary waves are initially centered at $X_s/d = -19.85 - \sqrt{\frac{4d}{3H}} \operatorname{arccosh} \sqrt{20}$. The simulation domain ($x \in [-100d, 15d]$) is subdivided into 920 mesh cells. At both ends of the simulation domain, open boundary conditions apply. In the simulations, $C_r = 0.7$ and $n = 0.01$ are used.

In Figs. 3 and 4, the computed water surface profiles by the SWE and SNH models at various time instances ($\tilde{t} = t\sqrt{gd}$) are respectively shown for the $H/d = 0.0185$ and $H/d = 0.28$ test cases. The experimental data of Synolakis [30] are also presented. As can be seen from Fig. 3, for the weak nonlinear test case, the wave running up (Fig. 3(a)–(d)) and retreating (Fig. 3(e)–(f)) processes are reasonably modeled and the numerical results match the experiment data fairly well. For this test case, the numerical predictions by the SWE and SNH models are indistinguishable. For the highly nonlinear case,

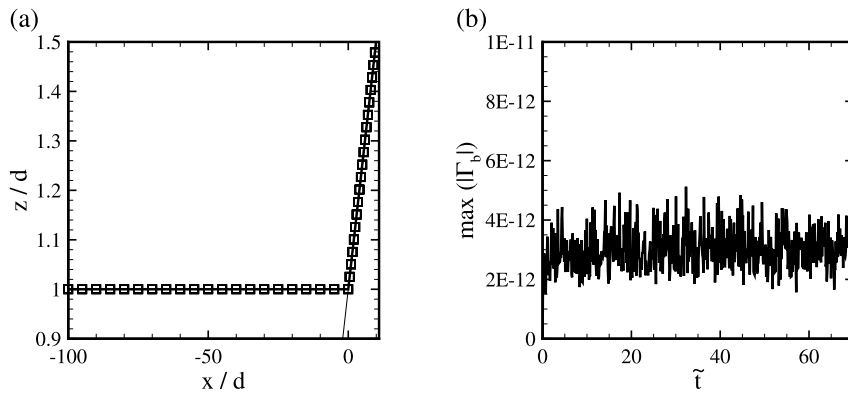


Fig. 5. Comparison of the computed water surface profile (—) with the analytic solution (\square) at $\tilde{t} = 70$ for the well-balanced test. The thin solid line represents the bed topography. In (b), the variation of maximum $|\Gamma_b|$ with time is shown.

as can be seen from Fig. 4(a) and (b), the wave amplitude and the wave phase results in the wave shoaling processes are predicted in close agreement with the measured data by the SNH model, while the wave amplitude is predicted significantly lower and the wave phase speed is predicted much larger by the SWE model; in the later times (Fig. 4(c) and (d)), the difference in the results between the SWE and SNH models can be neglected. In both test cases, the SWE and SNH models are all capable of capturing the wet–dry fronts with great accuracy.

The well-balanced property of the SNH model is tested here. In the simulation, all the simulation parameters are kept the same as those in the test above in this section except that, initially the flow is at rest and a constant water surface elevation $z = d$ is prescribed all over the simulation domain. In Fig. 5(a), the water surface profile computed by the SNH model at $\tilde{t} = 70$ along with the analytic solution is displayed. It is seen that the computed water surface profile matches the analytic solution exactly, suggesting that the numerical model is well-balanced. The reason is that under a quiescent flow condition, the dynamic pressure Γ_b and the vertical velocities w_s and w_b are negligible. In Fig. 5(b), the maximum absolute value of Γ_b in the simulation domain is displayed and it is seen that the Γ_b in the simulation domain is on the order of 10^{-12} and it does not grow with time. As a result, the terms on the right-hand side of Eq. (17) are too small to initialize a flow (actually these terms are divided by ρ ($= 1000 \text{ kg/m}^3$) in Eq. (17) to further minimize their effect to within machine accuracy).

3.3. Solitary waves running up a vertical wall

Experiments on solitary waves running up a vertical wall were conducted at the US Army Engineer Waterways Experiment Station [31]. The glass flume in the experiment was 23.2 m long by 0.45 m wide. The flume consists of a horizontal bottom region ($z_b = 0$) with length 15.04 m, followed by three plane beaches with different slopes (1:53, 1:150 and 1:13); a vertical wall is located at the end of the flume. The sketch of the flume is shown in Fig. 6. Ten capacitance wave gauges (part of their locations are shown in Fig. 6) were utilized in the experiment to record the surface wave elevations along the centerline of the flume. The offshore still water depth is $d = 0.218 \text{ m}$.

Two cases with different wave-height-to-water-depth ratios, $H/d = 0.039$ and $H/d = 0.264$, are considered here. These test cases were used by Wei and Jia [16] to validate their SNH model developed using a finite-element scheme. Following Wei and Jia [16], the grid resolution is chosen so that at least 100 mesh cells are distributed in one wave length and thus $\Delta x \approx 0.05 \text{ m}$ and 0.02 m are respectively used in the simulations for the two test cases. The value of C_r is set to 0.25 to resolve the rapid transformations of the waves. The roughness coefficient is set to $n = 0.01$. The observed data at Gauge 5 provides a reference for the adjustment of the timing of the computed waveforms.

Figs. 7 and 8 show the time series of the water surface elevations computed by the SWE and SNH models at different wave gauge locations for the two test cases. As can be seen from Fig. 7, two wave peaks occur at all the four wave gauge locations; the two wave peaks respectively correspond to the periods when the wave travels eastwards to interact with the vertical wall and when the wave is reflected back and travels westwards. For the weak nonlinear test case ($H/d = 0.039$), the computed results match the measured data reasonably well; the difference in the results predicted by the SWE and SNH models is small at all the four wave gauge locations, with the wave amplitude and wave phase results more accurately predicted by the SNH model. We also observe that the numerical predictions at Gauges 7–9 slightly deviate from the measured data in the later times after the wave is reflected back; this may be attributed to the experimental setup [16]. The numerical predictions for the highly nonlinear test case, as illustrated in Fig. 8, are similar to that for the weak nonlinear case (see Fig. 7), but the wave after being reflected back from the vertical wall for the highly nonlinear case becomes irregular and various small-amplitude waves are generated. Generally, the numerical results simulated by the SNH model for the highly nonlinear test case match the observed data well. From Fig. 8, it is clear that the SWE model cannot predict reasonable results for the highly nonlinear test case; for instance, the wave amplitude is predicted rather small compared with the measured data and the generation of small waves after the wave is reflected back cannot be well-predicted.

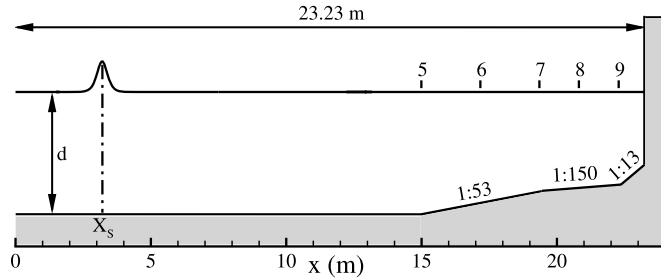


Fig. 6. Sketch for the solitary wave running up on a vertical wall test (not to scale). The shaded area shows the bed topography.

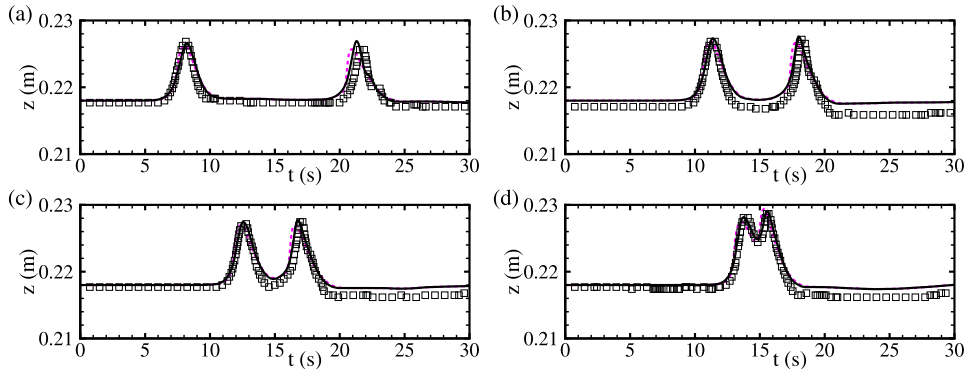


Fig. 7. Time series of the computed water surface elevation at Gauge 5 (a), Gauge 7 (b), Gauge 8 (c) and Gauge 9 (d) for the solitary wave running up a vertical wall test with $H/d = 0.039$. The solid line (—) in black and the dashed line (---) in pink show the computed results by the SNH and SWE models, respectively. The symbols (\square) show the experimental data by Synolakis [30]. (For interpretation of the references to color in this figure legend, the reader is referred to the web version of this article.)

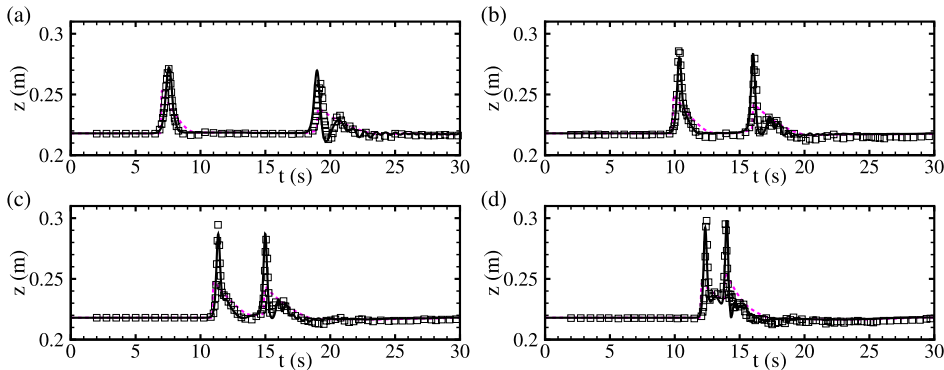


Fig. 8. Same as Fig. 7, but for the $H/d = 0.264$ test case.

4. Conclusions and discussion

In this study, a depth-averaged non-hydrostatic numerical model has been developed using the non-incremental pressure-correction method. Based on a semi-staggered grid, the numerical scheme is devised using a hybrid finite-volume and finite-difference method. A Godunov-type scheme is used in the hydrostatic step to allow capturing shocks automatically and thus to model the wave-breaking process well in the nearshore area. The developed numerical model is tested against several benchmark tests. The results show that the developed model is accurate, well-balanced and can model the wave propagation and transformation processes fairly well over irregular bed topography. Compared with the numerical results computed by the SWE model, the numerical predictions by the SNH model with considering the wave dispersion effect are significantly improved, especially for simulations with large wave-height-to-water-depth ratios.

The accurate prediction of the flow field is the basis for predicting the sediment transport and the morphological change processes, and in viewing that the SNH model is superior to the conventional SWE model in describing short wave motions in the nearshore area, we expect that the sediment motions can be more accurately predicted by combining the sediment

transport and bed deformation modules with the SNH model (compared with that combined with the SWE model) and this is left for future studies.

Acknowledgements

This study is part of the research project sponsored by the National Natural Science Foundation of China (Grant Nos. 51409195, 51379155), by the Fundamental Research Funds for the Central Universities (Grant No. 2042014kf0068) and by the China Postdoctoral Science Foundation (Grand No. 2014M550408).

Appendix A. Derivation of the non-hydrostatic pressure equation

In this appendix, a detailed derivation for Eq. (24) is given. Firstly, from Eq. (19), we have for cell i ,

$$(q_x)_i^{n+1} = (q_x)_i^m - \frac{\Delta t}{\Delta x} \frac{h_i^m}{2\rho} \left((\Gamma_b)_{i+1/2}^{n+1} - (\Gamma_b)_{i-1/2}^{n+1} \right) - \frac{\Delta t}{4\rho} \left((\Gamma_b)_{i+1/2}^{n+1} + (\Gamma_b)_{i-1/2}^{n+1} \right) \frac{\partial (z_i^m + (z_b)_i)}{\partial x} \quad (\text{A.1})$$

and for cell $i - 1$,

$$(q_x)_{i-1}^{n+1} = (q_x)_{i-1}^m - \frac{\Delta t}{\Delta x} \frac{h_{i-1}^m}{2\rho} \left((\Gamma_b)_{i-1/2}^{n+1} - (\Gamma_b)_{i-3/2}^{n+1} \right) - \frac{\Delta t}{4\rho} \left((\Gamma_b)_{i-1/2}^{n+1} + (\Gamma_b)_{i-3/2}^{n+1} \right) \frac{\partial (z_{i-1}^m + (z_b)_{i-1})}{\partial x} \quad (\text{A.2})$$

The subtraction of Eq. (A.2) from Eq. (A.1) and with the assumption $(q_x)_i^{n+1} \approx u_i^{n+1} h_i^m$, we have

$$u_i^{n+1} - u_{i-1}^{n+1} = u_i^m - u_{i-1}^m - \frac{\Delta t}{2\rho\Delta x} \left((\Gamma_b)_{i+1/2}^{n+1} - 2(\Gamma_b)_{i-1/2}^{n+1} + (\Gamma_b)_{i-3/2}^{n+1} \right) - \frac{\Delta t}{4\rho} \left\{ \frac{(\Gamma_b)_{i+1/2}^{n+1} + (\Gamma_b)_{i-1/2}^{n+1}}{h_i^m} \frac{\partial (z_i^m + (z_b)_i)}{\partial x} - \frac{(\Gamma_b)_{i-1/2}^{n+1} + (\Gamma_b)_{i-3/2}^{n+1}}{h_{i-1}^m} \frac{\partial (z_{i-1}^m + (z_b)_{i-1})}{\partial x} \right\} \quad (\text{A.3})$$

From Eq. (20), we obtain

$$(w_s)_{i-1/2}^{n+1} - (w_b)_{i-1/2}^{n+1} = -2(w_b)_{i-1/2}^{n+1} + (w_s)_{i-1/2}^n + (w_b)_{i-1/2}^n + 2\Delta t \frac{(\Gamma_b)_{i-1/2}^{n+1}}{\rho h_{i-1/2}^m} \quad (\text{A.4})$$

As seen from Eqs. (A.3) and (A.4), the velocity differences $u_i^{n+1} - u_{i-1}^{n+1}$ and $(w_s)_{i-1/2}^{n+1} - (w_b)_{i-1/2}^{n+1}$ are functions of the non-hydrostatic pressure at the new time level. Hence, by substituting Eqs. (A.3) and (A.4) into Eq. (23), the following elliptic equation for non-hydrostatic pressure is obtained

$$A_{i-1/2}(\Gamma_b)_{i-3/2}^{n+1} + B_{i-1/2}(\Gamma_b)_{i-1/2}^{n+1} + C_{i-1/2}(\Gamma_b)_{i+1/2}^{n+1} = S_{i-1/2} \quad (\text{A.5})$$

with coefficients given by

$$\begin{aligned} A_{i-1/2} &= -\frac{\Delta t}{2\rho\Delta x^2} + \frac{\Delta t}{4\rho h_{i-1}^m \Delta x} \frac{\partial (z_{i-1}^m + (z_b)_{i-1})}{\partial x} \\ B_{i-1/2} &= \frac{2\Delta t}{\rho(h_{i-1/2}^m)^2} + \frac{\Delta t}{\rho\Delta x^2} - \frac{\Delta t}{4\rho\Delta x} \left\{ \frac{1}{h_i^m} \frac{\partial (z_i^m + (z_b)_i)}{\partial x} - \frac{1}{h_{i-1}^m} \frac{\partial (z_{i-1}^m + (z_b)_{i-1})}{\partial x} \right\} \\ C_{i-1/2} &= -\frac{\Delta t}{2\rho\Delta x^2} - \frac{\Delta t}{4\rho h_i^m \Delta x} \frac{\partial (z_i^m + (z_b)_i)}{\partial x} \\ S_{i-1/2} &= -\frac{u_i^m - u_{i-1}^m}{\Delta x} + \frac{1}{h_{i-1/2}^m} \left\{ 2(w_b)_{i-1/2}^{n+1} - (w_s)_{i-1/2}^n - (w_b)_{i-1/2}^n \right\} \end{aligned} \quad (\text{A.6})$$

References

- [1] J.H. Sorensen, Hazard warning systems: review of 20 years of progress, *Nat. Hazards Rev.* 1 (2000) 119–125.
- [2] M. Guerra, R. Cienfuegos, C. Escauriaza, F. Marche, J. Galaz, Modeling rapid flood propagation over natural terrains using a well-balanced scheme, *J. Hydraul. Eng., ASCE* 140 (2014) 04014026.
- [3] J. Roelvink, I. Brøker, Cross-shore profile models, *Coast. Eng.* 21 (1993) 163–191.
- [4] Y. Hu, X. Guo, X. Lu, Y. Liu, R.A. Dalrymple, L. Shen, Idealized numerical simulation of breaking water wave propagating over a viscous mud layer, *Phys. Fluids* 24 (2012) 112104.
- [5] X. Lu, X. Zhang, B. Dong, H. Liu, B. Mao, Physical based numerical schemes for the discretization of the sediment settling term, *C. R., Méc.* 341 (2013) 581–591.
- [6] G.S. Stelling, M. Zijlema, An accurate and efficient finite-difference algorithm for non-hydrostatic free-surface flow with application to wave propagation, *Int. J. Numer. Methods Fluids* 43 (2003) 1–23.
- [7] J.A. Zelt, The run-up of nonbreaking and breaking solitary waves, *Coast. Eng.* 15 (1991) 205–246.
- [8] A.B. Kennedy, Q. Chen, J.T. Kirby, R.A. Dalrymple, Boussinesq modeling of wave transformation, breaking, and runup. I: 1D, *J. Waterw. Port Coast. Ocean Eng.* 126 (2000) 39–47.
- [9] P. Madsen, O. Sørensen, H. Schäffer, Surf zone dynamics simulated by a Boussinesq type model. Part I. Model description and cross-shore motion of regular waves, *Coast. Eng.* 32 (1997) 255–287.
- [10] M.V. McCabe, P.K. Stansby, D.D. Apsley, Random wave runup and overtopping a steep sea wall: shallow-water and Boussinesq modelling with generalised breaking and wall impact algorithms validated against laboratory and field measurements, *Coast. Eng.* 74 (2013) 33–49.
- [11] F. Shi, J.T. Kirby, J.C. Harris, J.D. Geimana, S.T. Grilli, A high-order adaptive time-stepping TVD solver for Boussinesq modeling of breaking waves and coastal inundation, *Ocean Model.* 43 (2012) 36–51.
- [12] M. Tissier, P. Bonneton, F. Marche, F. Chazel, D. Lannes, A new approach to handle wave breaking in fully non-linear Boussinesq models, *Coast. Eng.* 67 (2012) 54–66.
- [13] M. Kazolea, A.I. Delis, C.E. Synolakis, Numerical treatment of wave breaking on unstructured finite volume approximations for extended Boussinesq-type equations, *J. Comput. Phys.* 271 (2014) 281–305.
- [14] Y. Yamazaki, Z. Kowalik, K.F. Cheung, Depth-integrated, non-hydrostatic model for wave breaking and run-up, *Int. J. Numer. Methods Fluids* 61 (2009) 473–497.
- [15] R.A. Walters, A semi-implicit finite element model for non-hydrostatic (dispersive) surface waves, *Int. J. Numer. Methods Fluids* 49 (2005) 721–737.
- [16] Z. Wei, Y. Jia, Simulation of nearshore wave processes by a depth-integrated non-hydrostatic finite element model, *Coast. Eng.* 83 (2014) 93–107.
- [17] S. Bryson, Y. Epshteyn, A. Kurganov, G. Petrova, Well-balanced positivity preserving central-upwind scheme on triangular grids for the Saint-Venant system, *ESAIM: Math. Model. Numer. Anal.* 45 (2011) 423–446.
- [18] X. Lu, B. Dong, B. Mao, X. Zhang, A robust and well-balanced numerical model for solving the two-layer shallow water equations over uneven topography, *C. R., Méc.* 343 (2015) 429–442.
- [19] C.W. Shu, S. Osher, Efficient implementation of essentially non-oscillatory shock-capturing schemes, *J. Comput. Phys.* 77 (1988) 439–471.
- [20] F.R. Fiedler, J.A. Ramirez, A numerical method for simulating discontinuous shallow flow over an infiltrating surface, *Int. J. Numer. Methods Fluids* 32 (2000) 219–239.
- [21] A. Harten, P.D. Lax, B. van Leer, On upstream differencing and Godunov-type schemes for hyperbolic conservation laws, *SIAM Rev.* 25 (1983) 35–61.
- [22] E.F. Toro, M. Spruce, W. Speares, Restoration of the contact surface in the HLL-Riemann solver, *Shock Waves* 4 (1994) 25–34.
- [23] E. Audusse, F. Bouchut, M.O. Bristeau, R. Klein, B. Perthame, A fast and stable well-balanced scheme with hydrostatic reconstruction for shallow water flows, *SIAM J. Sci. Comput.* 25 (2004) 2050–2065.
- [24] B. van Leer, Towards the ultimate conservative difference scheme. V. A second-order sequel to Godunov's method, *J. Comput. Phys.* 32 (1979) 101–136.
- [25] P.L. Roe, M.J. Baines, Algorithms for advection and shock problems, in: 4th GAMM Conference on Numerical Methods in Fluid Mechanics, Vieweg, Braunschweig, 1982, pp. 281–290.
- [26] L. Fraccarollo, E.F. Toro, Experimental and numerical assessment of the shallow water model for two-dimensional dam-break type problems, *J. Hydraul. Res.* 33 (1995) 843–864.
- [27] B. Yu, Y. Kawaguchi, W. Tao, H. Zoe, Checkerboard pressure predictions due to the underrelaxation factor and time step size for a nonstaggered grid with momentum interpolation method, *Numer. Heat Transf., Part B* 41 (2002) 85–94.
- [28] I.A. Svendsen, *Introduction to Nearshore Hydrodynamics*, World Scientific, Singapore, 2006.
- [29] H.A. van de Vorst, Bi-CGSTAB: a fast and smoothly converging variant of Bi-CG for the solution of nonsymmetric linear systems, *SIAM J. Sci. Comput.* 13 (1992) 631–644.
- [30] C.E. Synolakis, The runup of solitary waves, *J. Fluid Mech.* 185 (1987) 523–545.
- [31] M.J. Briggs, C.E. Synolakis, U. Kanoglu, D.R. Green, Runup of solitary waves on a vertical wall, in: *Long Wave Runup Models: Proceedings of the International Workshop*, World Scientific, Singapore, Friday Harbor, San Juan Island, WA, USA, 1995, pp. 375–383.